20. Hartman, R. C. *et al.* The third EGRET catalog of high-energy gamma-ray sources. *Astrophys. J. Suppl.* **123,** 79–202 (1999).
21. Rybichi, G. B. & Lightman, A. P. *Radiation Processes in Astrophysics* (Wiley and Sons, New York, 1979).
22. Mathis, J. S., Mezger, P. J. & Panagia, N. Interstellar radiation field and dust temperatures in the diffuse interstellar matter and in giant molecular clouds. *Astron. Astrophys.* **128,** 212–229 (1983).
23. Walsh, A. J., Hyland, A. R., Robinson, G. & Burton, M. G. Studies of ultracompact HII regions—I. Methanol maser survey of IRAS-selected sources. *Mon. Not. R. Astron. Soc.* **291,** 261–278 (1997).
24. Aharonian, F. A., Atoyan, A. M. & Kifune, T. Inverse Compton gamma radiation of faint synchrotron X-ray nebulae around pulsars. *Mon. Not. R. Astron. Soc.* **291,** 162–176 (1997).
25. Sikora, M., Begelman, M. C. & Rees, M. J. Comptonization of diffuse ambient radiation by a relativistic jet: The source of gamma rays from blazars. *Astrophys. J.* **421,** 153–162 (1994).
26. Enomoto, R. *et al.* Design study of CANGAROO-III, stereoscopic imaging atmospheric Cherenkov telescopes for sub-TeV gamma-ray detection. *Astropart. Phys.* **16,** 234–244 (2002).
27. Enomoto, R., *et al.* in *Proc. 27th Int. Cosmic Ray Conf. (Hamburg)* (eds Simon, M., Lorenz, E. & Pohl, M.) Vol. 6, 2477–2480 (Copernics Gesellschaft e.V., Katlenburg-Lindau, Germany, 2001).
28. Aharonian, F. A. *et al.* The energy spectrum of TeV gamma rays from the Crab nebula as measured by the HEGRA system of imaging air Cerenkov telescopes. *Astrophys. J.* **539,** 317–324 (2000).
29. Ishizaki, Y.. *Spectra and Large-scale Isotropy of the Cosmic X-ray Background from ASCA observations* Thesis(Univ. Tokyo.

Acknowledgements

We thank H. Tomida for help in understanding the ASCA observational results, M. Seta for comments on molecular cloud density, and F. Aharonian for suggestions. This work was supported by a Grant-in-Aid for Scientific Research by the Japan Ministry of Education, Science, Sports and Culture, and the Australian Research Council.

Competing interests statement

The authors declare that they have no competing financial interests.

Correspondence and requests for materials should be addressed to R.E.
(e-mail: enomoto@icrr.u-tokyo.ac.jp).

Atomic-scale imaging of individual dopant atoms and clusters in highly *n*-type bulk Si

P. M. Voyles*, D. A. Muller*, J. L. Grazul*, P. H. Citrin* & H.-J. L. Gossmann†

* *Bell Laboratories, Lucent Technologies; and † Agere Systems, 700 Mountain Avenue, Murray Hill, New Jersey 07974, USA*

As silicon-based transistors in integrated circuits grow smaller, the concentration of charge carriers generated by the introduction of impurity dopant atoms must steadily increase. Current technology, however, is rapidly approaching the limit at which introducing additional dopant atoms ceases to generate additional charge carriers because the dopants form electrically inactive clusters[1]. Using annular dark-field scanning transmission electron microscopy, we report the direct, atomic-resolution observation of individual antimony (Sb) dopant atoms in crystalline Si, and identify the Sb clusters responsible for the saturation of charge carriers. The size, structure, and distribution of these clusters are determined with a Sb-atom detection efficiency of almost 100%. Although single heavy atoms on surfaces or supporting films have been visualized previously[2–4], our technique permits the imaging of individual dopants and clusters as they exist within actual devices.

Future generations of Si technology[5,6] require free-electron densities in excess of 10^{21} electrons cm^{-3}. In some cases, this corresponds to concentrations of dopant atoms more than two orders of magnitude greater than their solid-solubility limit. Metastable growth techniques have significantly extended dopant concentrations beyond this limit, but the associated free-electron densities are still found to be no higher than $\sim 5 \times 10^{20}$ electrons cm^{-3} (ref. 7). (Confining the dopants to a two-dimensional layer may help to sidestep this restriction in cases where very high-temperature processing is not required[8].) It is therefore important to understand just how the dopant atoms become electrically inactive, leading to the observed saturation of free-electron densities.

Two generic models for electrically deactivating defect structures have been proposed for group V dopants in Si (that is, electron donors). The first model consists of between one and four dopant donor atoms surrounding a Si vacancy[9–14], and the second consists of only two donor atoms bound to reconfigured Si with no vacancies[15]. Determining which type of deactivating defect is formed in Si will establish how the fundamental limits to the free-electron concentration are reached.

We have used annular dark-field scanning transmission electron microscopy (ADF-STEM) to study highly Sb-doped Si. The samples were prepared by low-temperature molecular beam epitaxy, which provides high concentrations of Sb without introducing large amounts of Sb precipitates or Si vacancies[16]. The Sb density in the samples is 9.35×10^{20} atoms cm^{-3}, measured by Rutherford backscattering. The free-electron density from Hall measurements is 6.5×10^{20} electrons cm^{-3}, indicating that ~30% of the dopants are electrically inactive.

The STEM used here is state-of-the-art and has been optimized for very high stability during imaging[17], but the real key to observing individual Sb atoms lies in the cross-section sample preparation. Simulations show that for a Si column containing a single Sb atom to be more than 25% brighter than a pure Si column, the sample must be less than 50 Å thick. Random variations in thickness must be less than the contrast of one Sb atom, and the surfaces must be free from native amorphous SiO_2 layers and damaged bulk Si layers amorphized during thinning. These rigorous requirements are achieved using chemical-mechanical polishing techniques and an etch to remove the surface oxide as described in the Methods section. We do not use ion milling due to the unavoidable damage from implantation that could be mistaken for dopant clusters.

Figure 1 is an ADF-STEM image of a cross-section of the sample in the ⟨110⟩ zone-axis orientation. The brightest dots on the left are atomic columns containing at least one Sb atom. The undoped region on the right shows no such very bright dots. Two images,

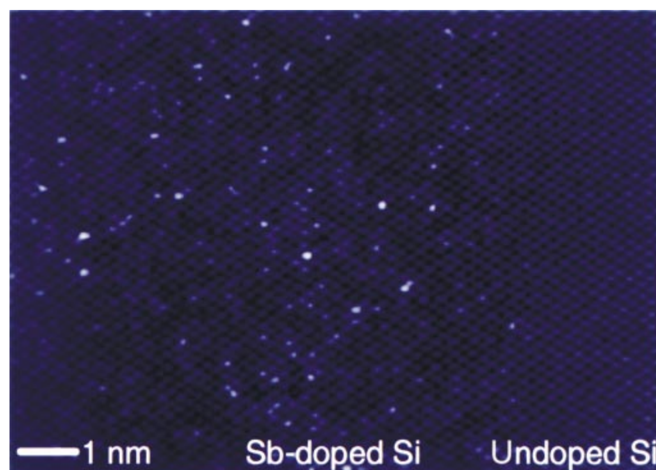

Figure 1 Annular dark-field scanning transmission electron microscopy image of a cross-section of highly Sb-doped Si. The brightest dots (left) are atomic columns containing one or more Sb atoms, absent in substrate (right), where there is no Sb. Thickness variations along the wedge have been subtracted using a second-order polynomial fit. The image has been low-pass filtered to remove scan noise, and is displayed with a nonlinear intensity scale to highlight bright features.

 © 2002 Macmillan Magazines Ltd

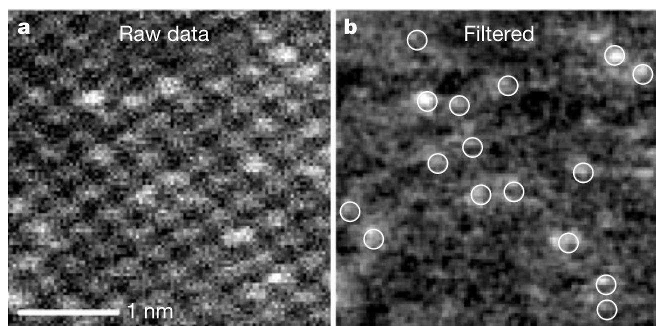

Figure 2 Segment from one of the analysed images (y) **a**, Raw data with no filtering, smoothing, or interpolation. **b**, The same region after filtering to remove the lattice. The circles indicate the Sb atoms, which are identified by the particle counting software.

Table 1 Number of atomic columns containing 0 to 2 Sb atoms

Number of Sb atoms	Image x (120 × 120 Å^2)		Image y (169 × 169 Å^2)	
	Predicted	Measured	Predicted	Measured
0	1,300	1,300 (50)	2,234	2,240 (70)
1	223	230 (30)	468	470 (40)
2	17	15 (15)	45	20 (20)

Predictions are based on equation (1). Measured values are the areas of the gaussian peaks in Fig. 3 with one standard deviation error derived from errors in the fit parameters given in parentheses. The large error in the measured values for two Sb atoms is due to the large uncertainties in the widths of the peaks.

described below and referred to as x and y, were obtained from Sb-doped regions of more uniform thickness. Images x and y were processed as described in the Methods section to identify the positions and intensities of the Sb-containing columns. A segment from image y before and after processing is shown in Fig. 2.

We find that the intensity and distribution of the Sb-occupied columns are consistent with a random substitution of Sb in Si sites, imaged with single-Sb-atom sensitivity and with almost 100% detection efficiency. For randomly distributed Sb atoms, the probability that a single column contains s Sb atoms is given by the binomial distribution:

$$P_{n,c}(s) = \frac{n!}{s!(n-s)!} c^s (1-c)^{n-s} \qquad (1)$$

where n is the number of Si and Sb atoms in the column and c is the fractional Sb concentration in the sample. Images x and y have total areas of 127 × 127 Å^2 and 169 × 169 Å^2 and contain 1,540 and 2,747 columns, respectively. The sample thicknesses, independently measured by comparing convergent-beam electron-diffraction patterns with multi-slice electron-scattering simulations[18], are 15 and 23 Å, corresponding to 9 and 11 Si atoms per column. As discussed below (and summarized in Table 1), the measured number of single-Sb-occupied columns in both images is in excellent agreement with predictions from equation (1). We also observe very few columns containing two Sb atoms, again consistent with predictions, because our samples are so thin.

ADF-STEM images are sometimes called Z-contrast[19,20] because the intensity scattered by an atom scales approximately as the atomic number $Z^{1.7}$ (close to the asymptotic Rutherford scattering limit of Z^2; ref. 21). Accordingly, one dopant Sb atom ($Z = 51$) should scatter about nine times more than one host Si atom ($Z = 14$). Such a large contrast might suggest that the Sb-occupied columns will exhibit discrete intensities with a distribution following equation (1), but this is not the case. The fast electron probe is strongly channelled along the atom columns[22–24], so the intensity scattered by a substitutional impurity depends on its depth along the column. Simulations show that both the channelling effect and the intensity of a Sb atom vary linearly with depth up to ~100 Å, after which they exhibit damped oscillations. Simulations also indicate that a single Sb atom is not visible in phase-contrast high-resolution TEM, even after exit-wave reconstruction (see Supplementary Information).

Figure 3 displays histograms of the column intensities from images x and y. The intensities of columns containing no Sb atoms (circles) have gaussian distributions with widths determined by variations in sample thickness and surface conditions. The Sb-containing columns (squares) also have largely gaussian distributions, but exhibit enhanced tails on the high intensity side. The green-shaded peaks have maxima at intensities (normalized to the mean unoccupied column intensity) of 1.20 and 1.16 in x and y, respectively. These values correspond to the range of intensities expected for a single Sb atom in a column. The red-shaded, high-intensity tails of the distributions can be fitted with a second gaussian of similar width, centred near twice the excess intensity of the single-Sb-atom peaks, that is, 1.40 and 1.32, respectively. The areas under the Si- and Sb-containing peaks are in extremely good agreement with the predictions of equation (1), as shown in Table 1. The detection error from noise and false positives is 3%.

Our results pass three reality checks for imaging individual atoms: (1) We count a number of dopant atoms that is consistent

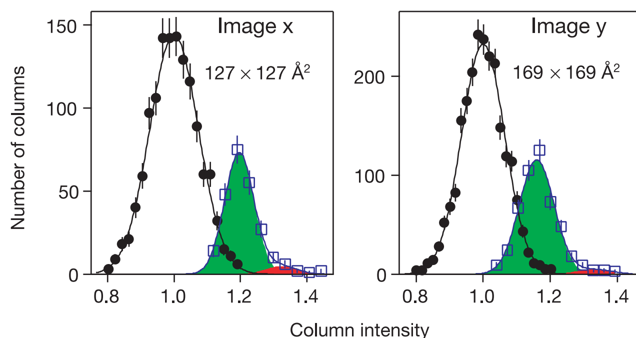

Figure 3 Histograms of atomic column intensities in two filtered images (x and y) from a highly Sb-doped Si sample. The images are different sizes and come from sample regions of different thickness. Filled circles denote columns with no Sb atoms, open squares denote columns containing Sb atoms. The error bars are $\pm\sqrt{N}$, where N is the number of columns in each intensity interval. Intensities are normalized by the mean unoccupied column intensity. The green-shaded area represents columns containing one Sb atom; the red-shaded area represents columns containing two Sb atoms. The areas overlap because the Sb-column intensities depend on Sb-atom depth and because the image processing software uses a local, not global, background to detect objects.

© 2002 Macmillan Magazines Ltd

with an independent measure of the dopant-atom concentration (Table 1). (2) We measure image intensities that agree with a statistical model for the distribution of those dopant atoms (equation (1), Fig. 3 and Table 1). (3) The features we identify as single atoms in a doped region are not seen in an undoped region imaged under identical conditions (Fig. 1). We are unaware of any previous work on bulk-like crystals passing any of these tests.

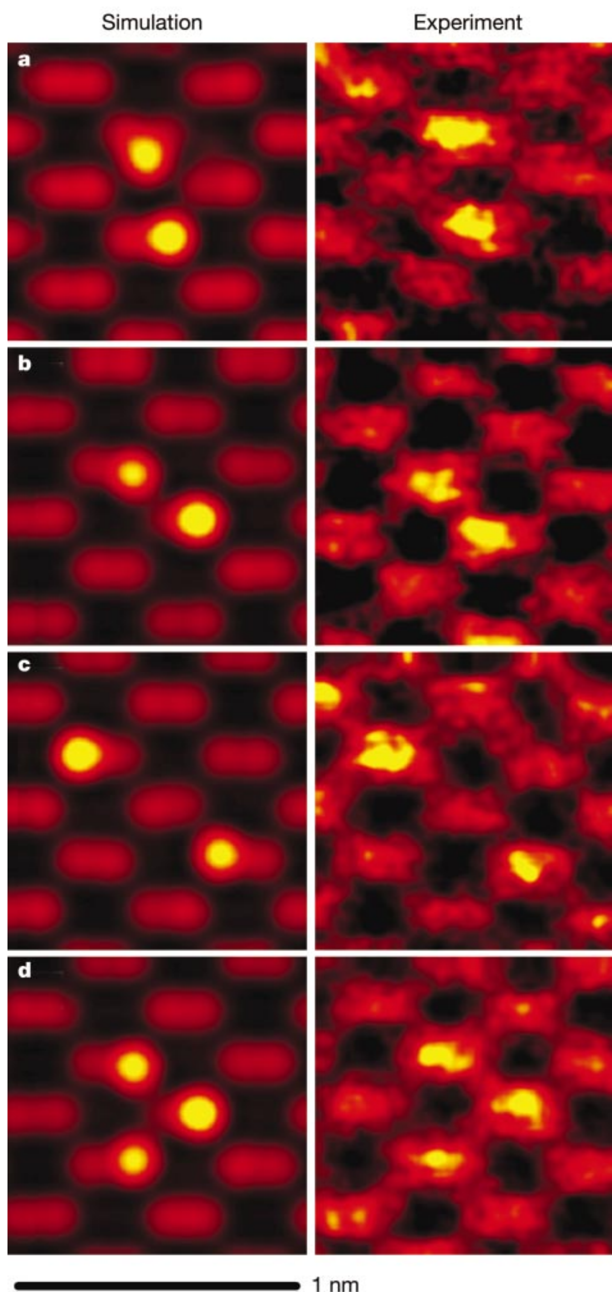

Figure 4 Simulated and experimental images of deactivating Sb clusters. The image intensity increases from black to red to yellow. Simulated images are shown on the left (see text for descriptions); **a**, DP2; **b**, DP2 viewed in a different projection; **c**, DP4; and **d**, Sb_3V. Selected experimental matches to simulated images are shown on the right. We note that (1) a Sb_2V projection also exists, similar to **a**; (2) projections of Sb_2V, and of Sb_3V with two Sb atoms in one column, each have images similar to **b**; (3) a Sb_4V projection with one doubly occupied column is similar to **d**; and (4) projections exist for DP2, Sb_2V, and DP4 with two Sb atoms in one column. Simulated images are based on structural models from ref. 15. Experimental images have been low-pass filtered to reduce noise and have had additional pixels added by interpolation (there were originally 12 pixels per column).

STEM images such as those on the right-hand side of Fig. 4 contain information for identifying different deactivating dopant clusters. The clusters are denoted Sb_iV (refs 9–14) for defect structures containing a Si vacancy V surrounded by $i = 2$, 3 or 4 Sb atoms, and DP2 or DP4 for donor-pair defects formed from two Sb atoms initially occupying either second- or fourth-nearest-neighbour sites in a {111} plane[15]. Our ability to identify particular defect structures is limited by two factors. First, STEM images view the structure in projection. Thus, for example, the ⟨110⟩ projections used here allow us to see only three of the four Sb atoms in a Sb_4V defect, but such an image is also consistent with one of the projections from a Sb_3V defect (see Fig. 4d). The electrical activity of a particular Sb atom cannot be firmly established for the same reason: what appears to be an inactive cluster-pair in the image could actually be two active Sb atoms at different depths. Second, the present limits of our instrumental resolution do not allow us to distinguish the small structural differences between the DP2 and Sb_2V defects (see Fig. 4a and b).

To overcome the projection problem, we have generated full three-dimensional structures using the image data and Monte Carlo simulation. Starting with the Sb-occupied column positions from the images, we populated each column with Sb atoms according to equation (1) and then placed those atoms at random depths. Nearest-neighbour Sb atoms were not allowed, consistent with X-ray absorption measurements[15]. The percentage of Sb atoms potentially involved in any one of the defect structures, and therefore the electrically inactive fraction, was then computed, subject to $\pm 3\%$ error from counting statistics.

We find that defects with two Sb next-nearest-neighbour atoms, which could be either Sb_2V or DP2, comprise 30 and 33% of the Sb atoms in images x and y. Both values are in excellent agreement with the Hall measurements (30%). DP4 defects account for 33 and 29%, in similarly good agreement. However, if we count both the Sb_2V or DP2 defects and the DP4 defects together, the electrically inactive fractions rise to unacceptably high values of 51 and 53%. This suggests that if DP2 and DP4 defects are both present, they cannot all be electrically inactive. Sb_3V and Sb_4V clusters are found to comprise only 1% of the Sb atoms.

From these results, we conclude that the primary deactivating defect in these samples contains only two Sb atoms. The paired defects outnumber the three- and four-atom clusters by roughly 50:1. Although our current data do not allow us to determine whether the primary pair defect is Sb_2V, DP2 or DP4, simulations indicate that atomic-resolution electron channelling experiments could tell us which defect is predominant. For example, in the DP2 structure, one of the Sb atoms is calculated to move significantly off its atomic column, while the other Sb atom remains essentially substitutional (this effect, seen in the simulation in Fig. 4a, is smaller than the scan noise in our STEM). In a Sb_2V structure, both atoms move symmetrically only a small distance towards the vacancy. Channelling draws the probe electrons tightly into the atom columns, so a Sb atom in a Sb_2V defect will scatter more strongly than the off-column Sb atom in a DP2 structure. Comparing ADF-STEM images acquired with different inner angles should highlight this effect, thereby allowing us to identify the deactivating defect. Alternatively, with the advent of aberration-corrected STEMs, these differences could be imaged directly[25]. □

Methods

Images were collected in a JEOL 2010F-ARP STEM operated with a 200-kV electron beam, a 10-mrad probe convergence half angle, and a 50-mrad ADF inner angle[17]. Samples were thinned using only double-wedge mechanical polishing with diamond-coated lapping film and colloidal silica. This is similar to the tripod polishing technique[26], but with better control. The amorphized surface layer produced by chemical-mechanical polishing is quickly oxidized. The oxide is stripped away with a 30-s etch in 100:1 hydrofluoric acid solution immediately before we place the sample in the STEM. The result is an essentially undamaged crystal matrix for viewing.

© 2002 Macmillan Magazines Ltd

Image processing

The periodic contribution from the Si lattice was filtered out of the images using a singular-value decomposition. The Sb atom positions were determined from the filtered images using Source Extractor software[27]. Source Extractor smoothed the input images with a 0.5-Å-wide gaussian, then identified collections of pixels with an area consistent with the point-spread function of the STEM (~1.6 Å wide, which is six pixels in image x and four pixels in image y) and 1.5 standard deviations (σ) per pixel above the local background as objects. The chance of a false atom detection from random noise is thus at the 9σ and 6σ levels, respectively. Consequently, the image statistics are not expected to be sensitive to precise threshold values. A 1.5σ threshold was chosen because it was the lowest value that did not produce false positives in the undoped region of Fig. 1. The detection error between 0 and 1 Sb atoms is 3%, which is largely due to remnant thickness variations.

Received 21 December 2001; accepted 28 March 2002.

1. Packan, P. A. Pushing the limits. *Science* **285,** 2079–2081 (1999).
2. Muller, E. W. Study of atomic structure of metal surfaces in the field ion microscope. *J. Appl. Phys.* **28,** 1–6 (1957).
3. Crewe, A. V., Wall, J. & Langmore, J. Visibility of single atoms. *Science* **168,** 1338–1340 (1970).
4. Nellist, P. D. & Pennycook, S. J. Direct imaging of the atomic configuration of ultradispersed catalysts. *Science* **274,** 413–415 (1996).
5. *International Technology Roadmap for Semiconductors, Update 2000* (International SEMATECH, Austin, Texas, 2000); see http://public.itrs.net/Files/2000UpdateFinal/2kUdFinal.htm.
6. Gossmann, H.-J., Rafferty, C. S. & Keys, P. Junctions for deep sub-100 nm MOS: How far will ion implantation take us? *Mater. Res. Soc. Symp.* **610,** B1.2.1–B1.2.10 (2000).
7. Williams, J. S. & Short, K. T. Metastable doping behavior in antimony-implanted (100) silicon. *J. Appl. Phys.* **53,** 8663–8667 (1982).
8. Citrin, P. H., Muller, D. A., Gossmann, H.-J., Vanfleet, R. & Northrup, P. A. Geometric frustration of 2D dopants in silicon: surpassing electrical saturation. *Phys. Rev. Lett.* **83,** 3234–3237 (1999).
9. Fair, R. B. & Weber, G. R. Effect of complex formation on diffusion of arsenic is silicon. *J. Appl. Phys.* **44,** 273–279 (1973).
10. Mathiot, D. & Pfister, J. C. Diffusion of arsenic in silicon: validity of the percolation model. *Appl. Phys. Lett.* **42,** 1043–1044 (1983).
11. Pandey, K. C., Erbil, A., Cargill, C. S., Boehme, R. F. & Vanderbilt, D. Annealing of heavily arsenic-doped silicon: electrical deactivation and a new defect complex. *Phys. Rev. Lett.* **61,** 1282–1285 (1988).
12. Lawther, D. W. *et al.* Vacancy generation resulting from electrical deactivation of arsenic. *Appl. Phys. Lett.* **67,** 3575–3577 (1995).
13. Ramamoorthy, M. & Pantelides, S. T. Complex dynamical phenomena in heavily arsenic doped silicon. *Phys. Rev. Lett.* **76,** 4853–4756 (1996).
14. Saarinen, K. *et al.* Identification of vacancy-impurity complexes in highly n-type Si. *Phys. Rev. Lett.* **82,** 1883–1886 (1999).
15. Chadi, D. J. *et al.* Fermi-level pinning defects in highly n-doped silicon. *Phys. Rev. Lett.* **79,** 4834–4837 (1997).
16. Gossmann, H.-J., Unterwald, F. C. & Luftman, H. S. Doping of Si thin films by low-temperature molecular beam epitaxy. *J. Appl. Phys.* **73,** 8237–8241 (1993).
17. Muller, D. A. & Grazul, J. Optimizing the environment for sub-0.2 nm scanning transmission electron microscopy. *J. Electron Microsc.* **50,** 219–226 (2001).
18. Kirkland, E. J. *Advanced Computing in Electron Microscopy* (Plenum, New York, 1998).
19. Howie, A. Image contrast and localized signal selection techniques. *J. Microsc.* **17,** 11–23 (1979).
20. Pennycook, S. J. & Narayan, J. Metastable doping behavior in antimony-implanted (100) silicon. *Appl. Phys. Lett.* **45,** 385–387 (1984).
21. Kirkland, E. J., Loane, R. F. & Silcox, J. Simulation of annular dark field STEM images using a modified multislice method. *Ultramicroscopy* **23,** 77–96 (1987).
22. Loane, R. F., Kirkland, E. J. & Silcox, J. Visibility of single heavy atoms on thin crystalline silicon in simulated annular dark field. *Acta Cryst. A* **44,** 912–927 (1988).
23. Hillyard, S. E. & Silcox, J. Thickness effects in ADF STEM zone-axis images. *Ultramicroscopy* **52,** 325–334 (1993).
24. Hillyard, S. E. & Silcox, J. Detector geometry, thermal diffuse scattering and strain effects in ADF STEM imaging. *Ultramicroscopy* **58,** 6–17 (1995).
25. Delby, N., Krivanek, O. L., Nellist, P. D., Batson, P. E. & Lupini, A. R. Progress in aberration-corrected scanning transmission electron microscopy. *J. Electron Microsc.* **50,** 177–185 (2001).
26. Klepeis, S. J., Benedict, J. P. & Anderson, R. M. in *Mater. Res. Soc. Proc.* (ed. Bravman, J. C.) 179–190 (Materials Research Society, Pittsburgh, 1988).
27. Bertin, E. & Arnouts, S. SExtractor: software for source extraction. *Astron. Astrophys. Suppl. Ser.* **117,** 393–404 (1996).

Supplementary Information accompanies the paper on *Nature*'s website (http://www.nature.com).

Acknowledgements

We thank P. Mithra for introducing us to singular value decomposition, E. Kirkland for sharing his STEM image simulation codes, and D. Wittman for help with the Source Extractor software.

Competing interests statement

The authors declare that they have no competing financial interests.

Correspondence and requests for materials should be addressed to D. A. M. (e-mail: davidm@bell-labs.com).

Molecular segregation observed in a concentrated alcohol–water solution

S. Dixit*, J. Crain*, W. C. K. Poon*, J. L. Finney† & A. K. Soper‡

* *Department of Physics and Astronomy, The University of Edinburgh, Mayfield Road, Edinburgh EH9 3JZ, UK*
† *Department of Physics and Astronomy, University College London, Gower Street, London WC1E 6BE, UK*
‡ *ISIS Facility, Rutherford Appleton Laboratory, Chilton, Didcot, Oxon OX11 OQX, UK*

When a simple alcohol such as methanol or ethanol is mixed with water[1,2], the entropy of the system increases far less than expected for an ideal solution of randomly mixed molecules[3]. This well-known effect has been attributed to hydrophobic headgroups creating ice-like or clathrate-like structures in the surrounding water[4], although experimental support for this hypothesis is scarce[5–7]. In fact, an increasing amount of experimental and theoretical work suggests that the hydrophobic headgroups of alcohol molecules in aqueous solution cluster together[2,8–10]. However, a consistent description of the details of this self-association is lacking[11–13]. Here we use neutron diffraction with isotope substitution to probe the molecular-scale structure of a concentrated alcohol–water mixture (7:3 molar ratio). Our data indicate that most of the water molecules exist as small hydrogen-bonded strings and clusters in a 'fluid' of close-packed methyl groups, with water clusters bridging neighbouring methanol hydroxyl groups through hydrogen bonding. This behaviour suggests that the anomalous thermodynamics of water–alcohol systems arises from incomplete mixing at the molecular level and from retention of remnants of the three-dimensional hydrogen-bonded network structure of bulk water.

In spite of considerable research into the nature of alcohol–water mixtures at the molecular level (see, for example, ref. 2 and several experiments and computer simulations[5,14–18]), there still seems to be little physical insight into the causes of the anomalous thermodynamic properties of alcohol–water mixtures. To investigate these matters, we perform a detailed determination of the methyl–methyl, methyl–water and water–water correlations in a concentrated mixture of methanol in water (7 methanol molecules:3 water molecules), using neutron diffraction with hydrogen isotope labelling. The diffraction data are interpreted by empirical potential structure refinement (EPSR; see Methods). Typical EPSR fits to our diffraction data on the methanol–water mixture are shown in Fig. 1. From the EPSR molecular ensembles, we derive site–site radial distribution functions (RDFs), $g_{\alpha\beta}(r)$, which describe the relative density of one type of atom, β, as a function of distance, r, from another type, α. (In this experiment, the labels α and β can each take on one of six possible atom types. They are C for methanol carbon, O for methanol oxygen, M for methyl hydrogen, H for hydroxyl hydrogen, O_W for water oxygen, and H_W for water hydrogen.) By comparing RDFs derived from our data with RDFs derived from previous diffraction data on pure methanol[19] and pure water[20], we examine how the local ordering of the methanol molecules is modified by the addition of small amounts of water. Although many of the individual site–site RDFs are not determined separately in the diffraction experiment (for example the O_W–O_W distribution), the EPSR procedure ensures that all the estimated RDFs are consistent with all the diffraction data.

The correlations between methanol molecules, as given by the $g_{CC}(r)$, $g_{MM}(r)$ and $g_{OO}(r)$ RDFs, are shown in Fig. 2 for both pure methanol and the concentrated aqueous mixture. Two notable features emerge: when water is added, the near-neighbour distance of the CC and MM functions shift to a lower radius by about 2% for

 © 2002 Macmillan Magazines Ltd